

# **Regenerative oscillation and four-wave mixing in graphene optoelectronics**

T. Gu<sup>1\*</sup>, N. Petrone<sup>1</sup>, J. F. McMillan<sup>1</sup>, A. van der Zande<sup>1</sup>, M. Yu<sup>2</sup>, G. Q. Lo<sup>2</sup>, D. L. Kwong<sup>2</sup>, J. Hone<sup>1</sup>, and C. W. Wong<sup>1\*</sup>

<sup>1</sup> Columbia University, New York, NY 10027, USA.

<sup>2</sup> The Institute of Microelectronics, 11 Science Park Road, Singapore Science Park II  
Singapore 117685, Singapore.

Email: \* tg2342@columbia.edu and cww2104@columbia.edu

**The unique linear and massless band structure of graphene, in a purely two-dimensional Dirac fermionic structure, have led to intense research spanning from condensed matter physics [1-5] to nanoscale device applications covering the electrical [6-7], thermal [8-9], mechanical [10] and optical [11, 12] domains. Here we report three consecutive first-observations in graphene-silicon hybrid optoelectronic devices: (1) ultralow power resonant optical bistability; (2) self-induced regenerative oscillations; and (3) ultrafast coherent four-wave mixing, all at a few femtojoule cavity recirculating energies. These observations, in comparison with control measurements with solely monolithic silicon cavities, are enabled only by the dramatically-large and ultrafast  $\chi^{(3)}$  nonlinearities in graphene and the large  $Q/V$  ratios in wavelength-localized photonic crystal cavities. These results demonstrate the feasibility and versatility of hybrid two-dimensional graphene-silicon nanophotonic devices**

**for next-generation chip-scale ultrafast optical communications, radio-frequency optoelectronics, and all-optical signal processing.**

Sub-wavelength nanostructures in monolithic material platforms have witnessed rapid advances towards chip-scale optoelectronic modulators [13-16], photoreceivers [17-18], and high-bitrate signal processing architectures [19-20]. Coupled with ultrafast nonlinearities as a new parameter space for optical physics [21], breakthroughs such as resonant four-wave mixing [22] and parametric femtosecond pulse characterization [23-24] have been described. Recently, graphene – with its broadband dispersionless nature and large carrier mobility – has been examined for its gate-variable optical transitions [25-26] towards broadband ultrafast electroabsorption modulators [27] and photoreceivers [28-29], as well as saturable absorption for mode-locking [30]. Due to its linear band structure allowing interband optical transitions at all photon energies, graphene has been suggested as a material with large  $\chi^{(3)}$  nonlinearities [31]. In this Letter we demonstrate the exceptionally high nonlinear response of graphene with a wavelength-scale localized photonic crystal cavity, enabling ultralow power optical bistable switching, self-induced regenerative oscillations, and ultrafast coherent four-wave mixing at femtojoule cavity energies on the semiconductor chip platform. The structure examined is a hybrid graphene-silicon cavity (as illustrated in Figure 1), achieved by rigorous transfer of monolayer large-area graphene sheet onto air-bridged silicon photonic crystal nanomembranes with minimal linear absorption and optimized optical input/output coupling. This optoelectronics demonstration is complemented with recent examinations of large-area [32-33] graphene field-effect transistors and analog circuit designs [34] for potential large-scale silicon integration.

Figure 1 illustrates the graphene-cladded photonic crystal nanomembranes investigated. The optical nanocavity is a point-defect photonic crystal  $L3$  cavity (with three missing holes) [35-36], with nearest holes at the cavity edges tuned by  $0.15a$  (where  $a$  is the photonic crystal lattice constant). The  $L3$  cavity is side coupled to a photonic crystal line defect waveguide for optical transmission measurements. Chemical vapor deposition (CVD) grown graphene is wet-transferred onto the silicon nanomembrane [37, 38] (see Methods; and Supplementary Information, Section S1), with the graphene heavily  $p$ -doped, on a large sheet without requiring precise alignment. As shown in Figure 1b, the single layer graphene is identified by Raman spectroscopy via the full-width half-maximum of the  $G$  and  $2D$  band peaks ( $34.9\text{ cm}^{-1}$  and  $49.6\text{ cm}^{-1}$  respectively) and the  $G$ -to- $2D$  peak intensity ratio of  $\sim 1$  to  $1.5$ . The  $G$  band lineshape is a single and symmetrical Lorentzian indicating good uniformity graphene [39]. Heavily doped graphene is specifically prepared to achieve optical transparency in the infrared with negligible linear losses, as the Fermi level is below the one-photon interband optical transition threshold [27] (Figure 1c inset) and intraband graphene absorption is near-absent in the infrared [40].

Transverse-electric (TE) polarization laser light is launched onto the optical cavity and evanescently coupled to the monolayer graphene. As shown in Figure 1d, the cavity transmission spectra, performed with tunable continuous-wave laser sources, shows a consistent and large resonance red-shift of  $1.2\text{ nm/mW}$ , approximately  $4\times$  larger than that of our near-identical control cavity without graphene. The low power “cold cavity” transmissions taken at  $2.5\text{ }\mu\text{W}$  input powers depict intrinsic  $Q$ s of 22,000 and loaded  $Q$ s of 7,500, with background Fabry-Perot oscillations arising from the input/output facet coupling reflections ( $\sim 0.12$  reflectivity). The high power cavity transmission is not only red-shifted to *outside* the cold cavity lineshape full-width

base but also exhibit a Fano-like asymmetric lineshape, with good matching to our coupled-mode model predictions (detailed in the Supplementary Information, Section S3). We also note that with the transferred monolayer graphene onto only the short photonic crystal regions the total fiber-chip-fiber transmission is decreased by less than 1 dB, slightly better than the 5-dB additional loss in recent modified graphene-fiber linear polarizers [40] (with different cavity or propagation lengths and evanescent core coupling). We emphasize that, for the same increased cavity power on a monolithic silicon cavity without graphene, both the control experiment and numerical models show a negligible thermal red-shift of 0.1 nm/mW, for the power levels and the specific loaded cavity  $Q^2/V$  values [of  $4.3 \times 10^7 (\lambda/n)^3$ ] investigated here.

The large frequency shifts from the graphene-cladded hybrid photonic cavity is next investigated for low-threshold optical bistability. Figure 2a shows the observed bistability at 100  $\mu$ W threshold powers for a loaded cavity  $Q$  of 7,500, with cavity – input laser detuning  $\delta$  of 1.5 [with  $\delta$  defined as  $(\lambda_{laser} - \lambda_{cavity})/\Delta\lambda_{cavity}$ , where  $\Delta\lambda_{cavity}$  is the cold cavity full-width half-maximum linewidth]. The steady-state bistable hysteresis at a detuning of 1.7 is also illustrated in Figure 2a. The dashed lines show the coupled-mode theory numerical predictions of the hybrid cavity, including first-order estimates of the graphene-modified thermal, linear and nonlinear loss, and free carrier parameters (detailed in the Supplementary Information, Section S2 and S3). We also note the heavily-doped graphene has a two-photon absorption at least several times larger than silicon, described by its isotropic bands for interband optical transitions [41], leading to increased free carrier densities/absorption and overall enhanced thermal red-shift.

To verify the bistable switching dynamics, we input time-varying laser intensities to the graphene-cladded cavity, allowing a combined cavity power – detuning sweep. Figure 2b shows

an example time-domain output transmission for two different initial detunings [ $\delta_{(t=0)} = -1.3$  and  $\delta_{(t=0)} = 1.6$ ] and for an illustrative triangular-waveform drive, with nanosecond resolution on an amplified photoreceiver. With the drive period at 77 ns, the observed thermal relaxation time is  $\sim 20$  ns. Cavity resonance dips (with modulation depths  $\sim 3$ -dB in this example) are observed for both positive detuning (up to 0.34 nm,  $\delta = 1.4$ ) and negative detuning (in the range from -0.15 nm ( $\delta = -0.75$ ) to -0.10 nm ( $\delta = -0.5$ )). The respective bistable high- and low-state transmissions are illustrated in the inset of Figure 2b, for each bistability switching cycle. Bistability with both detunings are observable – with the negative detuning, the carrier-induced (Drude) blue-shifted dispersion overshoots the cavity resonance from the drive frequency and then thermally pins the cavity resonance to the laser drive frequency (see Supplementary Information, Section S4). Since the free carrier lifetime of the hybrid media is about 200 ps and significantly lower than the drive pulse duration, these series of measurements are thermally dominated; the clear (attenuated) resonance dips on the intensity up-sweeps (down-sweeps) are due to the measurement sampling time shorter than the thermal relaxation timescale and a cooler (hotter) initial cavity temperature.

When the input laser intensity is well above the bistability threshold, the graphene-cavity system deviates from the two-state bistable switching and becomes oscillatory as shown in Figure 3a. Regenerative oscillation has only been suggested in a few prior studies, such as theoretically predicted in GaAs nanocavities with large Kerr nonlinearities [42] or observed in high- $Q$  ( $3 \times 10^5$ ) silicon microdisks [43]. These regenerative oscillations are formed between the competing phonon and free carrier populations, with slow thermal red-shifts ( $\sim 10$  ns timescales) and fast free-carrier plasma dispersion blue-shifts ( $\sim 200$  ps timescales) in the case of our graphene-silicon cavities. The self-induced oscillations across the drive laser frequency are

observed at threshold cavity powers of 0.4 mW, at  $\sim 9.4$  ns periods in these series of measurements which gives  $\sim 106$  MHz modulation rates, at experimentally-optimized detunings from  $\delta_{(t=0)} = 0.68$  to 1.12. We emphasize that, for a monolithic silicon  $L3$  cavity, such regenerative pulsation has not been observed nor predicted to be observable at a relatively modest  $Q$  of 7,500 (see Supplementary Information, Section S4). The temporal coupled-mode models for a conventional silicon photonic crystal cavity predict the threshold for regenerative oscillations to be at least 20 mW (even higher than our tunable laser output), with significant nonlinear absorption.

Figure 3b shows the input-output intensity cycles constructed from the temporal response measurements of a triangular-wave modulated 1.2 mW laser with a 2  $\mu$ s cycle. Clear bistability behavior is seen below the carrier oscillation threshold. The system transits to the regime of self-sustained oscillations as the power coupled into the cavity is above the threshold, by tuning the laser wavelength into cavity resonance. We show an illustrative numerical modeling in Figure 3c: the fast free-carrier response fires the excitation pulse (blue dashed line; start cycle)), and heat diffusion (red solid line) with its slower time constant determines the recovery to the quiescent state in the graphene-cladded suspended silicon membrane. The beating rate between the thermal and free carrier population is around 50 MHz, as shown in the inset of Figure 3d, with the matched experimental data and coupled-mode theory simulation. The beating gives rise to tunable peaks in the radio-frequency frequency spectra (Figure 3d; blue solid line), which are absent when the input power is below the oscillation threshold (grey dashed line). As a supplementary detail, we note that the model does not include a time varying cavity quality factor, considering the high power would usually broaden the cavity bandwidth.

To examine only the Kerr nonlinearity, next we performed degenerate four-wave mixing measurements on the hybrid graphene – silicon photonic crystal cavities as illustrated in Figure 4, with continuous-wave laser input. A lower-bound  $Q$  of 7,500 was specifically chosen to allow a  $\sim 200$  pm cavity linewidth within which the highly dispersive four-wave mixing can be examined. The input pump and signal laser detunings are placed within this linewidth, with matched TE-like input polarization, and the powers set at 600  $\mu$ W. Two example series of idler measurements are illustrated in Figure 4a and 4b, with differential pump and signal detunings respectively. In both series the parametric idler is clearly observed as a sideband to the cavity resonance, with the pump detuning ranging -100 pm to 30 pm and the signal detuning ranging from -275 pm to -40 pm, and from 70 pm to 120 pm. For each fixed signal- and pump-cavity detunings, the generated idler shows a slight intensity roll-off from linear signal (or pump) power dependence when the transmitted signal (or pump) power is greater than  $\sim 400$   $\mu$ W due to increasing free-carrier absorption effects (Supplementary Information, Figure S5). As illustrated in Figure 4a and 4b, the converted idler wave shows a four-wave mixing 3-dB bandwidth roughly matching the cavity linewidth when the pump laser is centered at the cavity resonance.

A theoretical four-wave mixing model with cavity field enhancement (Figure 4c and 4d) matches with these first graphene-cavity observations, and described in further detail in the Supplementary Information (Section S5). Based on the numerical model match to the experimental observations, the observed Kerr coefficient  $n_2$  of the graphene-silicon cavity ensemble is  $4.8 \times 10^{-17}$  m<sup>2</sup>/W, an order of magnitude larger than in monolithic silicon and GaInP-related materials [24], and two orders of magnitude larger than in silicon nitride [25]. Independently we also modeled the field-averaged effective  $\chi^{(3)}$  and  $n_2$  of the hybrid graphene-

silicon cavity, described as  $\overline{n_2} = \left(\frac{\lambda_0}{2\pi}\right)^d \frac{\int n^2(r) n_2(r) (|E(r) \times E(r)|^2 + 2|E(r) \times E(r)^*|^2) d^d r}{(\int n^2(r) |E(r)|^2 d^d r)^2}$ , where  $E(r)$  is

the complex fields in the cavity,  $n(r)$  is local refractive index,  $\lambda_0$  is the wavelength in vacuum, and  $d$  is the number of dimensions (3). As detailed in the Supplementary Information (Section 5), the computed  $n_2$  is at  $7.7 \times 10^{-17} \text{ m}^2/\text{W}$ , matching well with the observed four-wave mixing derived  $n_2$ . The remaining discrepancies arise from a Fermi velocity slightly smaller than the ideal values ( $\sim 10^6 \text{ m/s}$ ) in the graphene. As illustrated in Figure 4d for both measurement and theory, the derived conversion efficiencies are observed up to -30-dB in the unoptimized graphene-cavity, even at cavity  $Q$ s of 7,500 and low pump powers of 600  $\mu\text{W}$ . The highly-doped graphene with Fermi-level level in the optical transparency region is a pre-requisite to these observations. We note that for a silicon cavity without graphene the conversion efficiencies are dramatically lower (by more than 20-dB) as shown in dashed black line, and even below the pump/signal laser spontaneous emission noise ratio (dotted grey line) preventing four-wave mixing observation in a single monolithic silicon photonic crystal cavity until now.

We have demonstrated for the first time a hybrid graphene – silicon optical cavity for chip-scale optoelectronics, with observations ranging from resonant optical bistability for optical signal processing at femtojoule level switching per bit, to temporal regenerative oscillations for self-pulsation generation at record femtojoule cavity circulating powers, to graphene-cavity enhanced four-wave mixing at femtojoule energies on the chip. The transferred graphene on a wavelength-scale localized optical cavity enhances not only the thermal nonlinearities but also the ultrafast effective Kerr nonlinearity, suggesting a new parameter space for chip-scale optical physics and ultrafast optics in optical information processing.



## Methods

**Device fabrication:** The photonic crystal nanostructures are defined by 248 nm deep-ultraviolet lithography in the silicon CMOS foundry onto undoped silicon-on-insulator (100) substrates. Optimized lithography and reactive ion etching was used to produce device lattice constants of 420 nm, hole radius of  $124 \pm 2$  nm. The photonic crystal cavities and waveguides are designed and fabricated on a 250 nm silicon device thickness, followed by a buffered hydrofluoric wet-etch of the 1  $\mu$ m buried oxide to achieve the suspended photonic crystal nanomembranes.

Centimeter-scale graphene are grown on 25  $\mu$ m thick copper foils by chemical vapor deposition of carbon. The top oxide layer of copper is firstly removed in the hydrogen atmosphere (50 mTorr, 1000°C, 2 sccm H<sub>2</sub> for 15 min), then monolayer carbon is formed on copper surface (250 mTorr, 1000°C, 35 sccm CH<sub>4</sub>, 2 sccm H<sub>2</sub> for 30 min). The growth is self-limited once the carbon atom covers the Cu surface catalytic. Then single layer graphene is fast cooled down before moved out of chamber. Poly-methyl-methacrylate (PMMA) is then spun-casted onto the graphene and then the copper foil etch-removed by floating the sample in FeNO<sub>3</sub> solution. After the metal is removed, graphene is transferred to a water bath before subsequent transfer onto the photonic crystal membranes. Acetone dissolves the PMMA layer, and the sample is rinsed with isopropyl alcohol and dry baked for the measurements.

**Optical measurements:** Continuous-wave finely-tuned semiconductor lasers from 1520 to 1620 nm (200 kHz bandwidth and -20 dBm to 7 dBm powers) were used for the measurements. Lensed tapered fibers (Ozoptics) with polarization controller and integrated on-chip spot size converters are used. Without the graphene cladding (in the control sample), the total fiber-chip-

fiber transmission is  $\sim -10$  dB. The fiber to channel waveguide coupling is optimized to be 3 dB per input/output facet, with 1 to 2 dB loss from channel to photonic crystal waveguide coupling. The linear propagation loss for our air-cladded photonic crystal waveguide has been determined at 0.6 dB/mm; for a photonic crystal waveguide length of 0.12 mm, the propagation loss in the waveguide is negligible. The output is monitored by an amplified InGaAs photodetector (Thorlabs PDA10CF, DC-150 MHz bandwidth) and oscilloscope (WaveJet 314A, 100 MHz bandwidth, 3.5 ns rise time) for the time-domain oscillations. The four-wave mixing pump laser linewidth is 10 pm ( $\sim 12$  GHz). Confocal microscopy was used for the graphene Raman spectroscopic measurements with a 100 $\times$  (numerical aperture at 0.95) objective, pumped with a 514 nm laser.

**Numerical simulations:** The three dimensional finite-difference-time-domain (FDTD) method with sub-pixel averaging is used to calculate the real and imaginary parts of the  $E$ -field distribution for the cavity resonant mode. The spatial resolution is set at 1/30 of the lattice constant (14 nm). Time-domain coupled mode theory including dynamic free carrier and thermal dispersion is carried out with 1 picosecond temporal resolution.

## References

- [1] Y. Zhang, Y.-W. Tan, H. L. Stormer, and P. Kim, Experimental observation of the quantum Hall effect and Berry's phase in graphene, *Nature* **438**, 201 (2005).
- [2] A. K. Geim and K. S. Novoselov, The rise of graphene, *Nature Materials* **6**, 183 (2007).
- [3] X. Du, I. Skachko, F. Duerr, A. Luican, and E. Y. Andre, Fractional quantum Hall effect and insulating phase of Dirac electrons in graphene, *Nature* **462**, 192 (2009).
- [4] C. R. Dean, A. F. Young, P. Cadden-Zimansky, L. Wang, H. Ren, K. Watanabe, T. Taniguchi, P. Kim, J. Hone, and K. L. Shepard, Multicomponent fractional quantum Hall effect in graphene, *Nature Physics* **7**, 693 (2011).
- [5] C. Berger, Z. Song, X. Li, X. Wu, N. Brown, C. Naud, D. Mayou, T. Li, J. Hass, A. N. Marchenkov, E. H. Conrad, P. N. First, and W. A. de Heer, Electronic Confinement and Coherence in Patterned Epitaxial Graphene, *Science* **312**, 1191 (2006).
- [6] I. Meric, M. Y. Han, A. F. Young, B. Ozyilmaz, P. Kim, and K. L. Shepard, Current saturation in zero-bandgap, top-gated graphene field-effect transistors, *Nature Nanotechnology* **3**, 654 (2008).
- [7] Y.-M. Lin, C. Dimitrakopoulos, K. A. Jenkins, D. B. Farmer, H.-Y. Chiu, A. Grill, and Ph. Avouris, 100-GHz transistors from wafer-scale epitaxial graphene, *Science* **327**, 662 (2010).
- [8] J. H. Seol, I. Jo, A. L. Moore, L. Lindsay, Z. H. Aitken, M. T. Pettes, X. Li, Z. Yao, R. Huang, D. Broido, N. Mingo, R. S. Ruoff, L. Shi, Two-dimensional phonon transport in supported graphene, *Science* **328**, 213 (2010).
- [9] N. M. Gabor, J. C. W. Song, Q. Ma, N. L. Nair, T. Taychatanapat, K. Watanabe, T. Taniguchi, L. S. Levitov, and P. Jarillo-Herrero, Hot carrier-assisted intrinsic photoresponse in graphene, *Science* **334**, 648 (2011).
- [10] C. Lee, X. Wei, J. W. Kysar, and J. Hone, Measurement of the elastic properties and intrinsic strength of monolayer graphene, *Science* **321**, 385 (2008).
- [11] F. Bonaccorso, Z. Sun, T. Hasan, and A. C. Ferrari, Graphene photonics and optoelectronics, *Nature Photonics* **4**, 611 (2010).
- [12] C.-F. Chen, C.-H. Park, B. W. Boudouris, J. Horng, B. Geng, C. Girit, A. Zettl, M. F. Crommie, R. A. Segalman, S. G. Louie, and F. Wang, Controlling inelastic light scattering quantum pathways in graphene, *Nature* **471**, 617 (2011).

- [13] Q. Xu, B. Schmidt, S. Pradhan, and M. Lipson, Micrometre-scale silicon electro-optic modulator, *Nature* **435**, 325 (2005).
- [14] A. Liu, R. Jones, L. Liao, D. Samara-Rubio, D. Rubin, O. Cohen, R. Nicolaescu, and M. J. Paniccia, A high-speed silicon optical modulator based on a metal-oxide-semiconductor capacitor, *Nature* **427**, 325 (2005); A. Liu, L. Liao, D. Rubin, H. Nguyen, B. Ciftcioglu, Y. Chetrit, N. Izhaky, and M. Paniccia, High-speed optical modulation based on carrier depletion in a silicon waveguide, *Optics Express* **15**, 660 (2007).
- [15] J. Liu, M. Beals, A. Pomerene, S. Bernardis, R. Sun, J. Cheng, L. C. Kimerling, and J. Michel, Waveguide-integrated, ultralow-energy GeSi electro-absorption modulators, *Nature Photonics* **2**, 7 (2008).
- [16] Y.-H. Kuo, Y. K. Lee, Y. Ge, S. Ren, J. E. Roth, T. I. Kamins, D. A. B. Miller, and J. S. Harris, Strong quantum-confined Stark effect in germanium quantum-well structures on silicon, *Nature* **437**, 1334 (2005).
- [17] S. Assefa, F. Xia, and Y. A. Vlasov, Reinventing germanium avalanche photodetector for nanophotonic on-chip optical interconnects, *Nature* **464**, 80 (2010).
- [18] Y. Kang, H.-D. Liu, M. Morse, M. J. Paniccia, M. Zadka, S. Litski, G. Sarid, A. Pauchard, Y.-H. Kuo, H.-W. Chen, W. S. Zaoui, J. E. Bowers, A. Beling, D. C. McIntosh, X. Zheng, and J. C. Campbell, Monolithic germanium/silicon avalanche photodiodes with 340 GHz gain–bandwidth product, *Nature Photonics* **3**, 59 (2009).
- [19] A. Biberman, S. Manipatruni, N. Ophir, L. Chen, M. Lipson, and K. Bergman, First demonstration of long-haul transmission using silicon microring modulators, *Optics Express* **18**, 15544 (2010).
- [20] M. Pelusi, F. Luan, T. D. Vo, M. R. E. Lamont, S. J. Madden, D. A. Bulla, D.-Y. Choi, B. Luther-Davies, and B. J. Eggleton, Photonic-chip-based radio-frequency spectrum analyser with terahertz bandwidth, *Nature Photonics* **3**, 139 (2009).
- [21] P. Colman, C. Husko, S. Combrie, I. Sagnes, C. W. Wong, and A. De Rossi, Temporal solitons and pulse compression in photonic crystal waveguides, *Nature Photonics* **4**, 862 (2010).
- [22] F. Morichetti, A. Canciamilla, C. Ferrari, A. Samarelli, M. Sorel, and A. Melloni, Travelling-wave resonant four-wave mixing breaks the limits of cavity-enhanced all-optical wavelength conversion, *Nature Communications* **2**, 296 (2011).
- [23] M. A. Foster, R. Salem, D. F. Geraghty, A. C. Turner-Foster, M. Lipson, and A. L. Gaeta, Silicon-chip-based ultrafast optical oscilloscope, *Nature* **456**, 81 (2008).

- [24] A. Pasquazi, M. Peccianti, Y. Park, B. E. Little, S. T. Chu, R. Morandotti, J. Azaña, and D. J. Moss, Sub-picosecond phase-sensitive optical pulse characterization on a chip, *Nature Photonics* **5**, 618 (2011).
- [25] F. Wang, Y. Zhang, C. Tian, C. Girit, A. Zettl, M. Crommie, and Y. R. Shen, Gate-variable optical transitions in graphene, *Science* **320**, 206 (2008).
- [26] Z. Q. Li, E. A. Henriksen, Z. Jiang, Z. Hao, M. C. Martin, P. Kim, H. L. Stormer, and D. N. Basov, Dirac charge dynamics in graphene by infrared spectroscopy, *Nature Physics* **4**, 532 (2008).
- [27] M. Liu, X. Yin, E. Ulin-Avila, B. Geng, T. Zentgraf, L. Ju, F. Wang, and X. Zhang, A graphene-based broadband optical modulator, *Nature* **474**, 64 (2011).
- [28] T. Mueller, F. Xia, and P. Avouris, Graphene photodetectors for high-speed optical communications, *Nature Photonics* **4**, 297 (2010).
- [29] F. Xia, T. Mueller, Y.-M. Lin, A. Valdes-Garcia, and P. Avouris, Ultrafast graphene photodetector, *Nature Nanotechnology* **4**, 839 (2009).
- [30] Z. Sun, T. Hasan, F. Torrisi, D. Popa, G. Privitera, F. Wang, F. Bonaccorso, D. M. Basko, and A. C. Ferrari, Graphene mode-locked ultrafast laser, *ACS Nano* **4**, 803 (2010).
- [31] E. Hendry, P. J. Hale, J. Moger, A. K. Savchenko, and S. A. Mikhailov, Coherent nonlinear optical response of graphene, *Phys. Rev. Lett.* **105**, 097401 (2010).
- [32] X. Li, W. Cai, J. An, S. Kim, J. Nah, D. Yang, R. Piner, A. Velamakanni, I. Jung, E. Tutuc, S. K. Banerjee, L. Colombo, and R. S. Ruoff, Large-area synthesis of high-quality and uniform graphene films on copper foils, *Science* **324**, 1312 (2009).
- [33] S. Bae, H. Kim, Y. Lee, X. Xu, J.-S. Park, Y. Zheng, J. Balakrishnan, T. Lei, H. R. Kim, Y. I. Song, Y.-J. Kim, K. S. Kim, B. Özyilmaz, J.-H. Ahn, B. H. Hong, and S. Iijima, Roll-to-roll production of 30-inch graphene films for transparent electrodes, *Nature Nanotechnology* **5**, 574 (2010).
- [34] Y.-M. Lin, A. Valdes-Garcia, S.-J. Han, D. B. Farmer, I. Meric, Y. Sun, Y. Wu, C. Dimitrakopoulos, A. Grill, P. Avouris, and K. A. Jenkins, Wafer-scale graphene integrated circuit, *Science* **332**, 1294 (2011).
- [35] X. Yang, M. Yu, D.-L. Kwong, and C. W. Wong, All-optical analogue to electromagnetically induced transparency in multiple coupled photonic crystal cavities, *Phys. Rev. Lett.* **102**, 173902 (2009).

- [36] Y. Akahane, T. Asano, B. Song, and S. Noda, High- $Q$  photonic nanocavity in a two-dimensional photonic crystal, *Nature* **425**, 944 (2003).
- [37] C. R. Dean, A. F. Young, I. Meric, C. Lee, L. Wang, S. Sorgenfrei, K. Watanabe, T. Taniguchi, P. Kim, K. L. Shepard, and J. Hone, Boron nitride substrate for high-quality graphene electronics, *Nature Nanotechnology* **5**, 722 (2010).
- [38] N. Petrone, C. R. Dean, I. Meric, AM van der Zande, P. Y. Huang, L. Wang, D. Muller, K. L. Shepard, and J. Hone, High-mobility scalable graphene by large-grain chemical vapor deposition growth, submitted under review (2012).
- [39] W. Zhao, P. H. Tan, J. Liu, and A. C. Ferrari, Intercalation of few-layer graphite flakes with FeCl<sub>3</sub>: Raman determination of Fermi level, layer by layer decoupling, and stability, *J. Am. Chem. Soc.* **133**, 5941 (2011).
- [40] M. Jablan, H. Buljan, and M. Soljačić, Plasmonics in graphene at infrared frequencies, *Phys. Rev. B* **80**, 245435 (2009).
- [41] Q. Bao, H. Zhang, B. Wang, Z. Ni, C. H. Y. X. Lim, Y. Wang, D. Yuan Tang, and K. P. Loh, Broadband graphene polarizer, *Nature Photonics* **5**, 411 (2011).
- [42] A. Armaroli, S. Malaguti, G. Bellanca, S. Trillo, A. de Rossi, and S. Combrié, Oscillatory dynamics in nanocavities with noninstantaneous Kerr response, *Phys. Rev. A* **84**, 053816 (2011).
- [43] T. J. Johnson, M. Borselli, and O. Painter, Self-induced optical modulation of the transmission through a high- $Q$  silicon microdisk resonator, *Optics Express* **14**, 817 (2006).

## **Acknowledgments**

We thank Alexander Gondarenko, Yilei Li, Joshua Lui, and Jinghui Yang for helpful discussions. We acknowledge funding support from NSF IGERT (DGE-1069240) and the Center for Re-Defining Photovoltaic Efficiency through Molecule Scale Control, an Energy Frontier Research Center funded by the U.S. Department of Energy, Office of Science, Office of Basic Energy Sciences under Award Number DE-SC0001085.

T.G., J.F.M. performed the experiments, T.G., N.P., A.V.D.Z., J.H. prepared the graphene transfer and synthesis, M.Y. G.Q.L., D.L.K. nanofabricated the membrane samples, T.G., C.W.W. performed the numerical simulations, and T.G., C.W.W. prepared the manuscript.

## **Additional information**

The authors declare no competing financial interests. Supplementary information accompanies this paper at [www.nature.com/naturephotonics](http://www.nature.com/naturephotonics). Reprints and permission information is available online at <http://www.nature.com/reprints/>. Correspondence and requests for materials should be addressed to T.G. and C.W.W.

**Figure captions:**

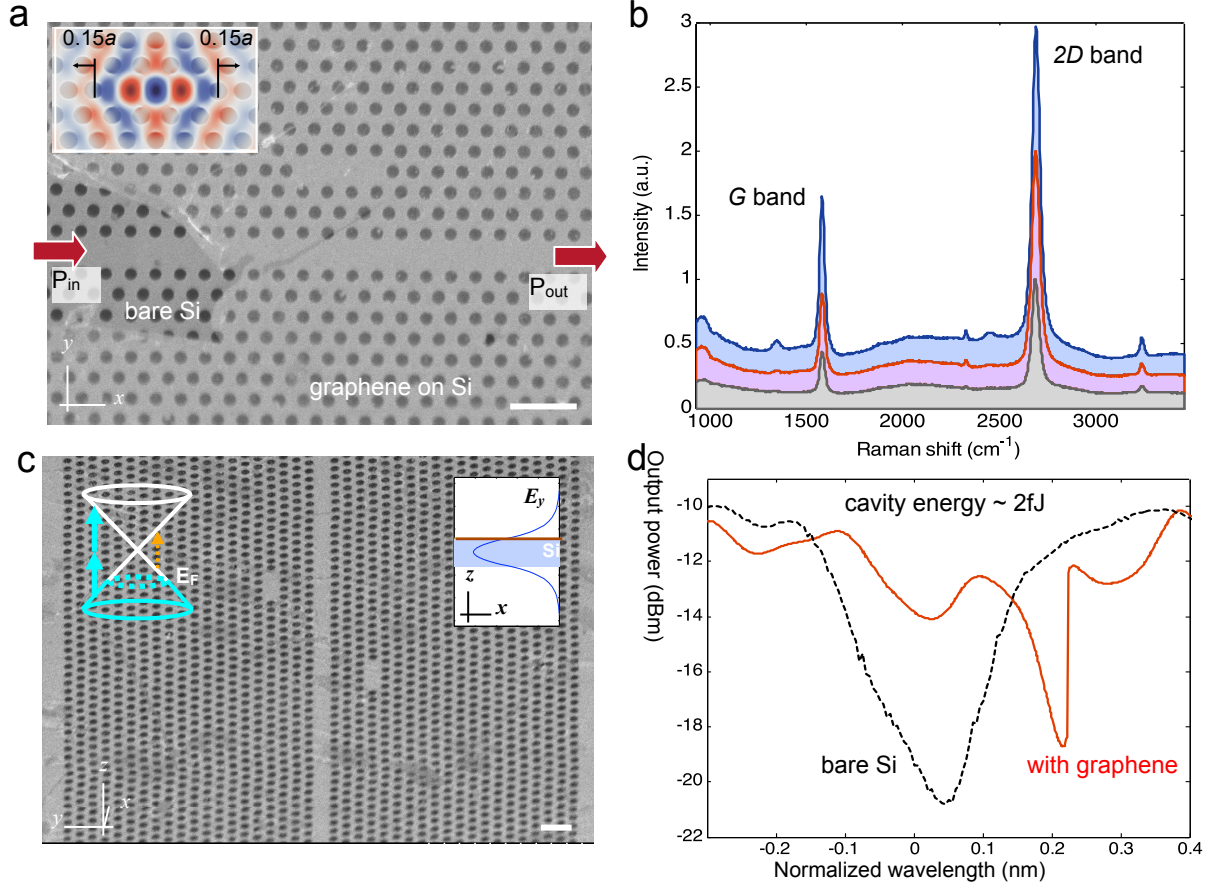


**Figure 1 | Graphene-cladded silicon photonic crystal nanostructures.** **a**, Scanning electron micrograph (SEM) of tuned photonic crystal cavity, with lattice constant  $a$  of 420 nm. Example SEM with separated graphene monolayer on silicon for illustration. Scale bar: 500 nm. Inset: example  $E_z$ -field from finite-difference time-domain computations. **b**, Measured Raman scattering spectra of monolayer CVD-grown graphene on photonic crystal cavity membrane. The Lorentzian lineshape full-width half-maximum of the  $G$  band ( $34.9 \text{ cm}^{-1}$ ) and  $2D$  band ( $49.6 \text{ cm}^{-1}$ ) peaks and the  $G$ -to- $2D$  peak ratio indicates the graphene monolayer, while the single symmetric  $G$  peak indicates good graphene uniformity. Homogeneity across the sample is



examined by exciting at different locations on the cavity membrane (blue, red and grey). **c**, SEM of suspended graphene-silicon membrane. Dark patches denote bilayer graphene. Left inset: Dirac cone illustrating the highly-doped Fermi level (dashed blue circle) allowing only two-photon transition (blue arrows) while the one-photon transition (orange dashed arrow) is forbidden. Right inset: Computed  $E_y$ -field along  $z$ -direction, with graphene at the evanescent top interface. Scale bar: 500 nm. **d**, Example measured graphene-cladded cavity transmission with asymmetric Fano-like lineshapes (red solid line), compared to a control bare Si cavity sample with symmetric Lorentzian lineshapes (black dashed line). Both spectra are measured at 0.6 mW input power, with similar intrinsic cavity quality factors between the graphene and the control sample. The cavity transmissions are centered to the intrinsic cavity resonances at low power (less than 100 uW input power).

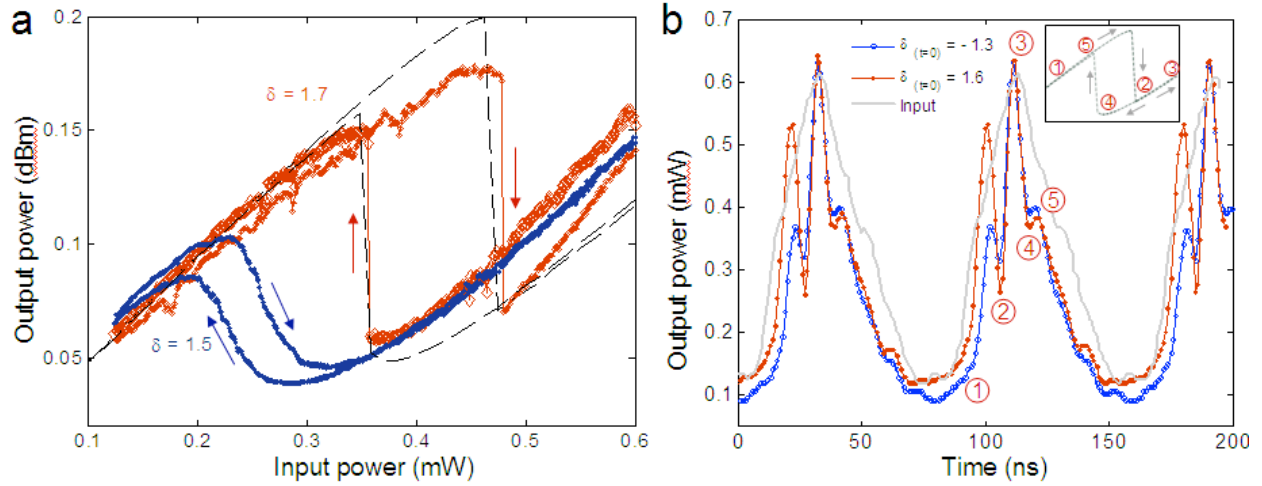


**Figure 2 | Bistable switching in graphene-cladded nanocavities.** **a**, Steady-state input/output optical bistability for the quasi-TE cavity mode with laser-cavity detuning  $\delta$  at 1.5 (blue) and 1.7 (red). The dashed black line is the coupled-mode theory simulation with effective nonlinear parameters of the graphene-silicon cavity sample. **b**, Switching dynamics with triangular waveform drive input (dashed grey line). The bistable resonances are observed for both positive and negative detuning. Blue empty circles:  $\delta(t=0) = -1.3$ , red solid circles:  $\delta(t=0) = 1.6$ . Inset: schematic of high- and low-state transmissions.

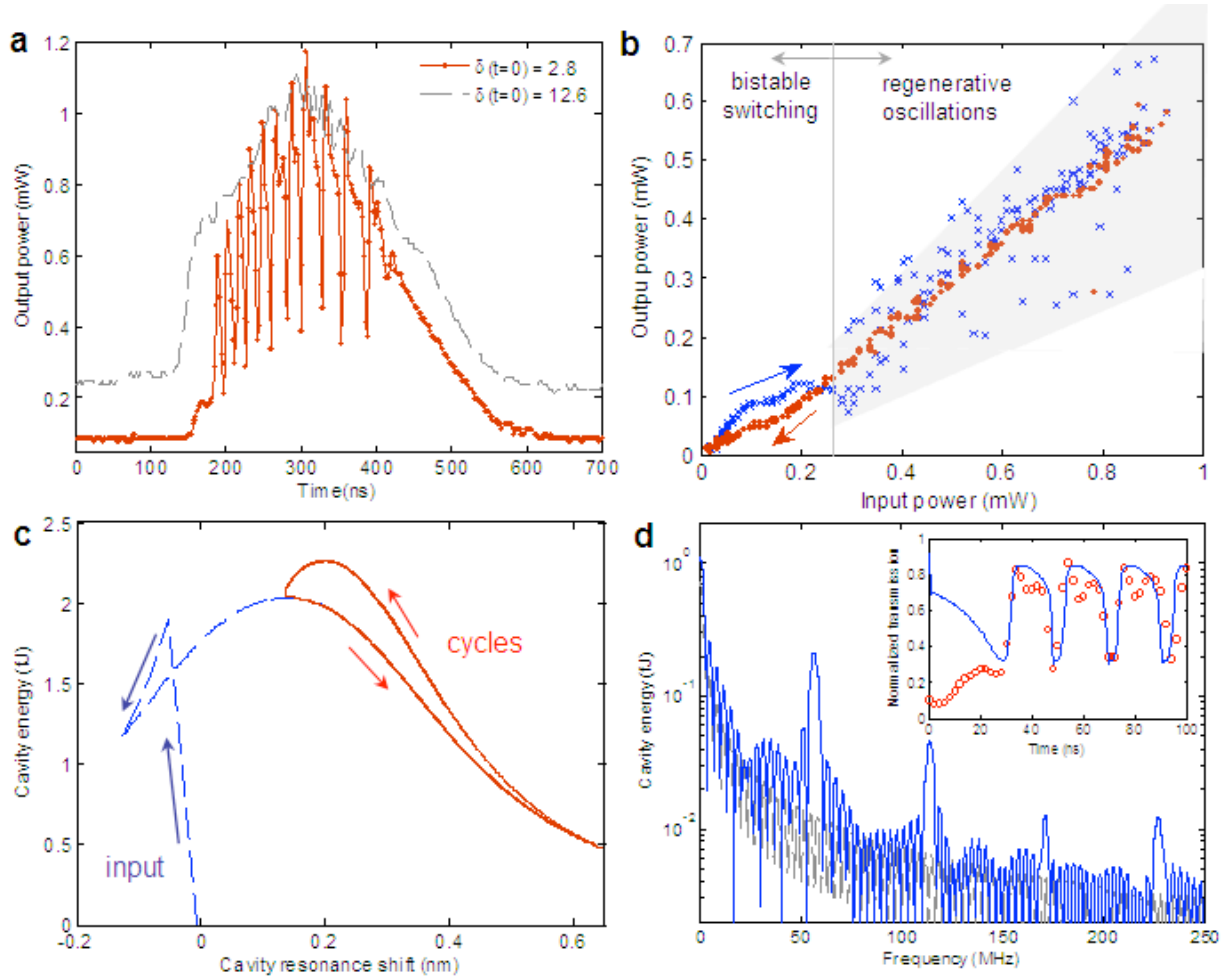


**Figure 3 | Regenerative oscillations in graphene-cladded nanocavities.** **a**, Observations of temporal regenerative oscillations in the cavity for optimized detuning (0.11 nm). The input power is quasi-triangular waveform with peak power 1.2 mW. The grey line is the reference output power, with the laser detuning 1.2 nm from cavity resonance. **b**, Mapping the output power versus input power with slow up (blue cross) and down (red) power sweeping. In the up-sweep process, the cavity starts to oscillate when the input power is beyond 0.2 mW, but the oscillation is not observed in the down-sweep process. **c**, Nonlinear coupled-mode theory model of cavity transmission versus resonance shift, in the regime of regenerative oscillations. With a detuning of 0.15 nm [ $\delta(t=0) = 0.78$ ] the free carrier density swings from  $4.4$  to  $9.1 \times 10^{17}$  per  $\text{cm}^3$

and the increased temperature circulates between 6.6 and 9.1K. **d**, Spectrum of cavity energy at below (0.2 mW, grey dashed line) and beyond oscillation threshold (0.6 mW, blue solid line) at the same detuning  $\delta(t=0) = 0.78$ , as in panel **c**. Inset: Normalized transmission from model (blue line) and experimental data at the same constant power level (red circles).

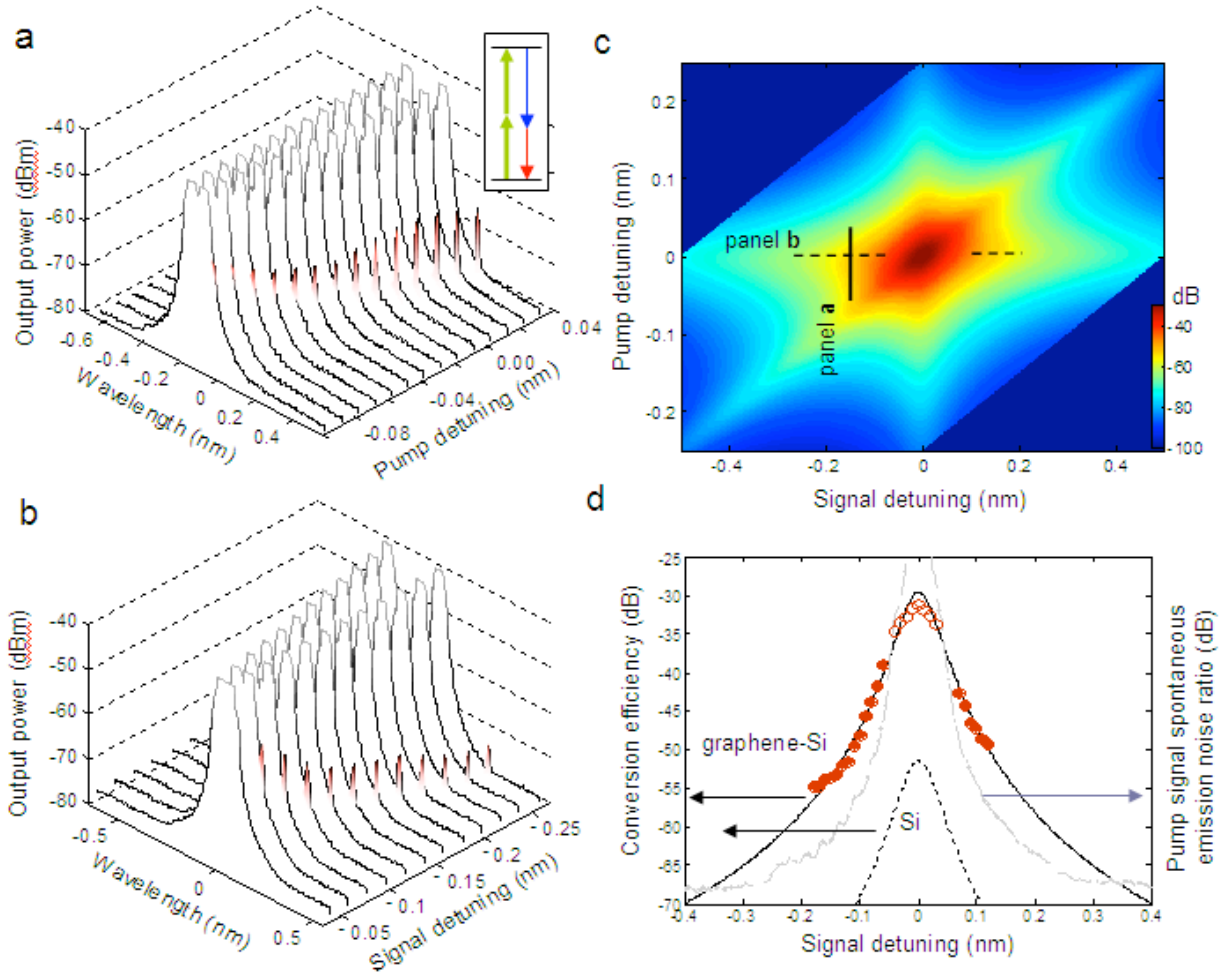


**Figure 4 | Parametric four-wave mixing in graphene-cladded silicon nanocavities. a,** Measured transmission spectrum with signal laser fixed at -0.16 nm according to cavity resonance, and pump laser detuning is scanned from -0.1 to 0.04 nm. Inset: band diagram of degenerate four-wave mixing process with pump (green), signal (blue) and idler (red) lasers. **b,** Measured transmission spectrum with pump laser fixed on cavity resonance, and signal laser detuning is scanned from -0.05 to -0.25 nm. **c,** Modeled conversion efficiency versus pump and signal detuning from the cavity resonance. The solid and dashed lines mark the region plotted in panel **a** and **b** respectively. **d,** Observed and simulated conversion efficiency of the cavity. Red solid dots are measured with signal detuning as in panel **b**, and the empty circles are obtained

through pump detuning as in panel **a**, plus 29.5-dB (off set due to the 0.16 nm signal detuning). Solid and dashed black lines are modeled conversion efficiencies of graphene-silicon and monolithic silicon cavities respectively. Grey dashed line (superimposed): illustrative pump/signal laser spontaneous emission noise ratio.